Exp Fluids (2007) 43:509–524
DOI 10.1007/s00348-007-0313-3

RESEARCH ARTICLE

Statistics of the surface temperature field of an air/water interface under air flow

T. A. Conover · J. R. Saylor

Received: 8 June 2006 / Revised: 6 April 2007 / Accepted: 6 April 2007 / Published online: 6 September 2007

Abstract Experimental results are presented that reveal the relationship between the root mean square of the surface temperature field of an air/water interface (σ) and the heat flux (q'') emanating from that interface, over a range of wind speeds. Experiments were conducted for wind speeds ranging from 1.0 to 4.0 m/s to determine if and how the σ versus q'' relationship was affected by wind speed. Consistent surfactant coverage conditions were maintained for wind speeds ranging from 1.0 to 2.6 m/s, and these are the focus of the results presented herein. For wind speeds above 2.6 m/s the surfactant was consistently pushed downstream, resulting in an inhomogeneous surface condition for the air/water interface. For wind speeds less than 2.6 m/s the relationship between σ and q'' is approximately linear and is weakly dependent on wind speed. The surface temperature field was obtained by infrared (IR) imaging. Sample IR images are presented in addition to the σ versus q'' data. IR images are presented for surfaces covered with insoluble surfactants (liquid phase and solid phase), a soluble surfactant, and a clean water surface.

1 Introduction

The transfer of heat across an air/water interface is relevant to the understanding of transport processes in lakes, rivers and oceans. When a warm water body is exposed to a relatively cooler layer of air above it, heat is transferred from the water to the air, via both evaporation and convection. This cools the water surface, creating an instability which results in natural convection in the water when the Rayleigh number in the water is sufficiently large. The Rayleigh number is defined as

$$Ra = \frac{g\beta\Delta TL^3}{\nu\alpha} \tag{1}$$

where β is the coefficient of thermal expansion, ν is the kinematic viscosity, α is the thermal diffusivity, ΔT is the characteristic temperature difference, and L is the characteristic length scale.

The fluid flow existing in the layer of water beneath an air/water interface that is transferring heat to its environment is an example of natural convection, which is turbulent for high Rayleigh numbers, the case considered here. Turbulent natural convection has traditionally been studied in a layer of fluid bounded above and below by solid plates, having either a constant temperature or constant heat flux boundary condition. There is a rich body of literature on this configuration, and excellent reviews have been published (Bodenschatz et al. 2000; Gettling 1998; Siggia 1994).

Herein we are concerned with the transport of heat in a fluid layer where the bottom boundary is solid and insulated, but the top boundary is an air/water interface. Heat transfer in this situation, referred to as free surface convection or evaporative convection, has received considerably less attention than the situation where both boundaries are solid. Sparrow and co-workers reported on the evaporation of water from a free surface for both natural convection and forced convection conditions (Sparrow et al. 1983; Prata and Sparrow 1985, 1986; Chuck and Sparrow 1987; Sparrow and Nunez 1988;

T. A. Conover · J. R. Saylor (✉)
Department of Mechanical Engineering,
Clemson University, Clemson, SC 29634-0921, USA
e-mail: jrsaylor@ces.clemson.edu

Nunez and Sparrow 1988). In these studies, the evaporation rate was quantified by the Sherwood number and was related to the Rayleigh number or Reynolds number in the air above the water surface. Natural convection experiments similar to those of Sparrow and co-workers were conducted earlier by Sharpley and Boelter (1938), and Boelter et al. (1946). Katsaros et al. (1977) experimentally obtained a relationship between the Nusselt number *Nu* and the Rayleigh number for turbulent natural convection in a tank of water, where both *Nu* and *Ra* were obtained using the temperature difference in the water (not the air as was the case for Sparrow, above).

In the free surface convection work described above, the goal was to obtain bulk parameterizations (e.g., *Nu–Ra* relationships), and no attempt was made to measure temperature fields or velocity fields. Such fields were obtained by Volino and Smith (1999) who studied the relationship of the surface temperature field of a water body undergoing evaporation, obtained via infrared imaging, to the velocity field of a plane located beneath and perpendicular to the water surface, obtained via PIV. Flack et al. (2001) obtained profiles of the fluctuating components of velocity beneath a water surface undergoing evaporation for similar conditions.

Saylor et al. (2000a, 2001) obtained experimental measurements of the surface temperature field of a body of water undergoing heat transfer to the air above it. These temperature fields were obtained via infrared (IR) imaging of the water surface and were used to reveal the relationship between the statistics of the surface temperature field (RMS and skewness) and the heat flux q'' for a body of water transferring heat to a quiescent air environment. This work consisted of laboratory experiments where a warm body of water was insulated on five sides, and allowed to transfer heat via evaporation and natural convection through the air/water interface to the overlaying air. Figure 1 is a plot of the root mean square (σ), of the surface temperature field, versus the heat flux through the surface, q'', obtained from that work, which reveals a linear relationship between these two variables. In addition to illustrating the variation of σ with q'', Fig. 1 also shows how the presence of a surfactant monolayer on the water surface affects σ. Figure 1 shows a slight reduction in σ when a surfactant monolayer is introduced onto the water surface. Natural water bodies are virtually always covered with surfactant monolayers, and hence the effect of these surfactants is important, as will be described later in this section.

The linear relationship between σ and q'' presented in Fig. 1 reveals a useful application of IR imagery. Because σ is obtained solely by processing IR images, this relationship suggests that the heat flux at a water surface can be obtained remotely, solely from IR imaging. For example, the heat flux emanating from a lake could conceivably be measured by an aircraft or satellite mounted IR camera. Such a method could have many uses in the study of energy and water balances in lakes and oceans. However, actual implementation of such a method, capable of accurate measurements of heat flux, would necessitate consideration of many complicating factors such as waves, depth sensitivity, currents, plumes, and (the subject of this work), wind.

Of especial interest here is the remote monitoring of nuclear reactor cooling ponds for treaty verification purposes. If the heat flux emanating from a cooling pond is known, then (with some knowledge of plant efficiency), a measure of the reactor power level can be ascertained, information critical to remote monitoring of these reactors. Methods currently exist that permit estimates of the heat flux emanating from such cooling ponds (Garrett and Hayes 1997; Garrett et al. 2000; Garrett 2002a, b). However, these methods are resource-intensive, requiring calibrated thermal imagery, local meteorological data and a 3-D hydrodynamic model. The results presented in Fig. 1 show how the RMS of the surface temperature field can be related to the surface heat flux without other measurements. One of the motivations of the present work is to ascertain if and how these laboratory results may be extended to remote measurements of cooling ponds.

It is noted that the range of heat fluxes presented in Fig. 1 are larger than those that would typically be found in natural lakes or over the ocean. However, the heat fluxes observed at power generation cooling ponds can be significantly larger than those existing in natural situations. For example, the heat fluxes observed over cooling ponds, averaged over the whole pond, tend to fall in the range 237–473 W/m^2 in the United States (Parker and Krenkel 1969). In the present work, we investigate fluxes as large as 2,000 W/m^2 since the fluxes can be larger near the discharge end of the cooling pond.

The results presented in Fig. 1 are all for the case of zero wind speed. The objective of the work presented herein was to determine how wind speed affects the statistics of the surface temperature field and to ascertain if and how these statistics may be used to measure heat flux for non-zero wind speed situations.

Water surfaces are highly prone to contamination by adventitious surfactant monolayers. Indeed, maintenance of a water surface which is free of such surfactants is a challenge, and surfactants are omnipresent on the surfaces of lakes and ponds. Surfactant monolayers are single molecule thick organic films that impart the property of elasticity at the water surface (Adamson 1990). A water surface completely free of monolayers (and externally imposed air flow) will have a shear-free boundary condition, while a surfactant-covered surface will have a constant elasticity

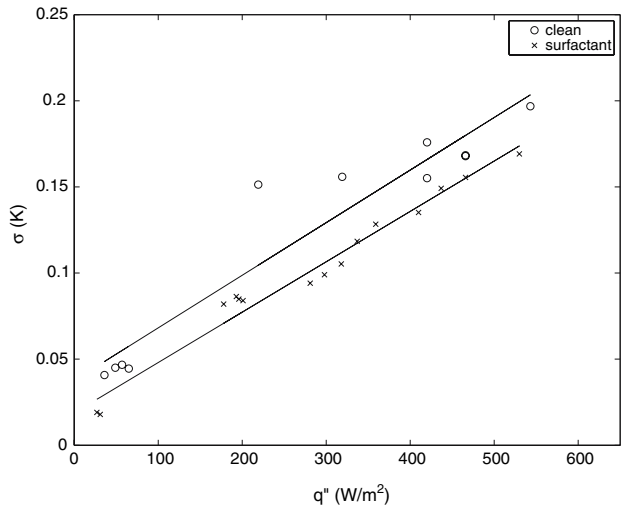

Fig. 1 Plot of the RMS σ of the surface temperature field of the air/water interface, versus the heat flux emanating from that air/water interface [Figure from Saylor et al. (2001)]. Clean and surfactant-covered conditions are presented. In the surfactant case, oleyl alcohol was used at a concentration of 0.11 μg/cm^2. Straight lines are linear best fits to each set of data. The air is quiescent, i.e., the wind speed is zero

boundary condition. The presence of elasticity in the surfactant-covered case damps velocity fluctuations near the water surface and thereby affects the surface temperature field. This is shown in Fig. 2 where surface temperature fields are presented for a clean and surfactant-covered surface where both surfaces have the same heat flux and are undergoing free surface natural convection at zero wind speed (Saylor et al. 2000a). The figure reveals significant differences in the length scale of the natural convection structures expressed in the surface temperature field. As noted earlier, the effect of the surfactant on the relationship between σ and q'' is relatively small, as evidenced by Fig. 1 (Saylor et al. 2001). Hence, although the presence of a surfactant effects a dramatic change in the length scale and the qualitative appearance of the surface temperature field, σ changes little, indicating that the temperature variations are not significantly altered. However, although the effect of surfactants on σ were found to be small at zero wind speed by Saylor et al. (2001), it is unclear if the same is true when the air above the water surface has a finite wind speed, and a side motivation of the present work was to address this point. Due to the omnipresent nature of surfactants in the environment, one might argue that the difference between clean versus surfactant-covered conditions is only of academic importance. In the results presented herein, it will be shown that the presence of wind can push surfactants downstream, creating a clean and surfactant-covered condition on the same water surface. While it is unclear if such conditions also exist in the field, it seems logical that they would, making the difference between clean and surfactant-covered conditions more important than might otherwise be the case.

2 Experimental method

2.1 Experimental facility

The experimental facility was an air/water tunnel consisting of a tank of warm water, and a simple wind tunnel located above the tank. This facility is illustrated in Fig. 3. The primary measuring instruments were a digital IR camera, a thermocouple data logger for measuring the bulk water temperature and a hand-held anemometer to measure wind speed.

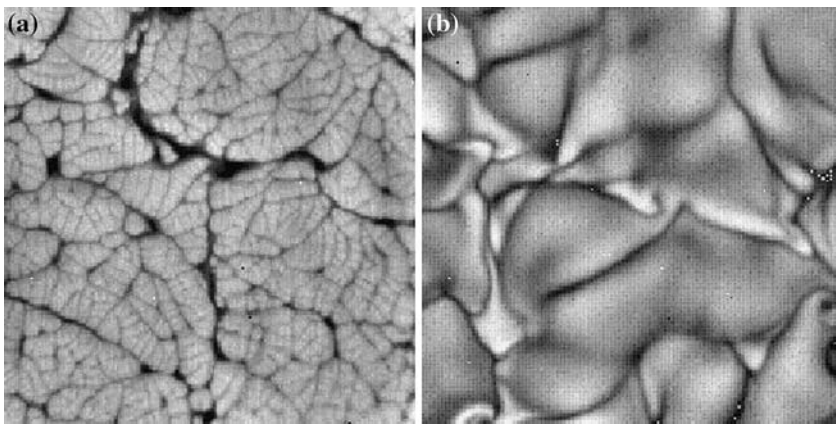

Fig. 2 Comparison of the surface temperature field for a body of water undergoing free surface natural convection for the case of **a** clean surface conditions, and **b** a surfactant-covered condition. The heat flux is 407 W/m^2 in both cases. Warm regions are white and cooler regions are *dark*. The surfactant is oleyl alcohol having a surface concentration of 0.11 μg/cm^2 in (**b**). Images obtained from Saylor et al. (2000a). The size of the two images is 17.1 and 15.7 cm for (**a**) and (**b**), respectively

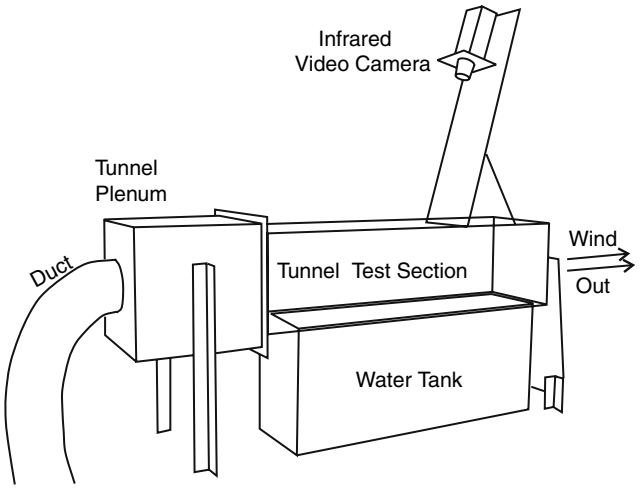

Fig. 3 Line drawing of the air/water tunnel. The *duct* indicated in the figure receives the positive pressure flow from the blower (not shown). The tunnel plenum was designed to provide a relatively uniform flow field across the face of the tunnel test section. The water tank indicated in the figure was always full during data taking

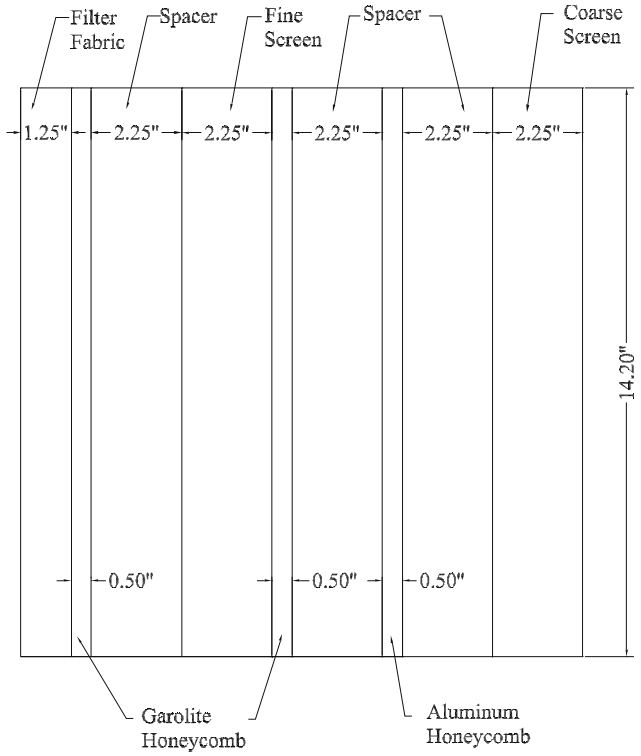

Fig. 4 Line drawing of the plenum portion of the air/water tunnel shown in Fig. 3

The water tank was constructed of plate glass, with inside dimensions of 100.3 cm along the wind direction, by 25.2 cm wide and 38.1 cm deep. The full volume of the tank was 96.5 l. The bottom and sides of the tank were covered with R-3 Styrofoam to minimize conduction heat loss. A thermocouple was mounted with the welded junction located at the geometric center of the tank to measure the bulk temperature (T_b) of the water. The thermocouple wire was sufficiently stiff to hold the position of the bead without additional support. Fig. 3 shows the infrared camera mounted on its stand on top of the test section. The camera is oriented at an angle of 16° from vertical to avoid observation of its own reflection in the water surface.

The wind tunnel portion of the air/water tunnel shown in Fig. 3 was constructed of clear polycarbonate. The entire wind tunnel fit snugly over the top of the water tank. Polycarbonate is opaque to infrared radiation, so a $6.5'' \times 6.5''$ square hole in the top of the test section was necessary to provide optical access for the infrared camera. The test section exhausted to the atmosphere, and the hole in the top of the test section was very near to atmospheric pressure, so there was minimal disturbance of the wind flow as confirmed by simulations performed using Fluent.

Figure 3 also shows the plenum box of the wind tunnel which was designed to condition the wind flow adequately while avoiding the difficulties associated with construction of a classic contraction section. The plenum box served to provide a uniform velocity profile across the entrance to the tunnel and is illustrated in Fig. 4.

The cross section of the wind tunnel portion of the air/water tunnel was $12''$ on a side. At 1.0 m/s wind, the growth of the laminar boundary layer on the middle of the test section wall was estimated to be 11 mm (at 90% velocity), with a displacement thickness of 5.7 mm. Thus the test section was wide enough to prevent wall effects from affecting the $10''$ wide water surface. The acceleration of the flow due to displacement was estimated to be $\sim 8\%$ of the inlet velocity at the middle of the tank and $\sim 11\%$ at the outlet. The measurement of nominal velocity was always taken at the geometric center of the wind tunnel outlet, so the nominal velocity at the middle of the test section where images were taken could be said to be a few percent lower than reported, due to displacement.

E-type thermocouples were used to measure characteristic temperatures at two locations: the bulk temperature T_b located in the center of the water tank, and the air temperature T_p (plenum temperature) located inside the plenum box of the wind tunnel. Temperatures were recorded by a two-channel data logger (Digi-Sense model 91100-50) having a stated accuracy of ±0.1% of the reading.

The nominal wind speed in the test section was measured using a Kestrel 1000 hand-held wind meter, with stated accuracy limits of ±3% of the reading and ±0.05 m/s (display resolution is 0.1 m/s). During measurement, the body introduces some blockage in the flow. Accordingly, it was mounted on a rod and always held consistently with the body fully in the flow, in order to make the blockage effect minimal and consistent.

The digital IR camera used to obtain images of the water surface was an Inframetrics ThermaCAM SC1000, a cooled-chip CCD camera sensitive to the 3.4–5 μm range of wavelengths with an NEΔT $<$ 0.07 K. The infrared camera produces a measurement of infrared radiation intensity (referred to as 'intensity' hereinafter), on an arbitrary scale. In order to measure the temperature of a surface, it is necessary to calibrate the camera output to known blackbody radiation as a function of temperature, and to know the emissivity of the measured surface. A simple thermal cavity calibrator was built for this purpose. During the calibration procedure, the calibrator was immersed in a constant temperature water bath, the camera was focused on the hole of the calibrator, and the water temperature was measured using an RTD (Minco, model 57929). Eight calibration images were taken at each of 12 nominal temperatures from 10 to 60°C. Figure 5 shows the result of these calibration runs. Each point shown is the average binary intensity from eight images at the given temperature. Typically the mean intensities of individual images varied by ±6 gray levels from the average. A fourth-order polynomial was fit to the calibration data. The norm of residuals of this fit was 26 gray levels, and the polynomial line passes within ±17 gray levels of each average intensity point. These errors are all very small compared to the range of the calibration. The resulting calibration function is

$$I(T) = 2.18499 \times 10^{-4}T^4 - 3.64606 \times 10^{-3}T^3 + 2.60526T^2 + 51.7340T + 8949.77, \quad (2)$$

where I is a 16-bit integer[1] and T is in °C.

The temperature of a radiating *blackbody* surface can be measured by inverting Eq. (2). Because the emissivity of the water surface ε is less than one, the intensity reported by the camera I_{12} combines emission at the water surface temperature T_s and reflection of the background radiation according to the equation

$$I_{12} = \varepsilon I(T_s) + (1 - \varepsilon)I(T_{Bk}), \quad (3)$$

where $I(T_{Bk})$ is the background intensity at temperature T_{Bk}, and is assumed to be blackbody radiation, for simplicity. The intensity function $I(T)$ is given according to Eq. (2). To determine ε for the water surface in the passband measured by the camera (3.4–5.0 μm), the tank (Fig. 3) was filled with water cooled slightly below room temperature to create a stably stratified body. The blower was turned off and the outlet end of the test section was blocked to further reduce air motion. The camera was installed on its 16° slanted stand, and focused on the image of a test target as seen reflected on the water surface. The test target was the bottom of an aluminum pan that was painted with flat black oil-based latex paint to approximate a blackbody surface. The pan was filled with water at a given temperature and well-stirred, with the temperature measured by a thermocouple. The pan temperature plays the role of T_{Bk} in this process. Images were taken at nine different test temperatures ranging from 5 to 45°C. Equation (3) was fit to all the data, solving for both ε and the unknown water surface temperature T_s. The result for this camera in this configuration is $\varepsilon = 0.981$. This value of ε is specific to the solid angle collected by the camera lens and is therefore not the hemispherical emissivity, but rather the emissivity specific to the geometry of this particular setup. Also, since the focal point of the camera is different for the setup where ε was measured and for the actual experiments, there is some error incurred, but this is expected to be small.

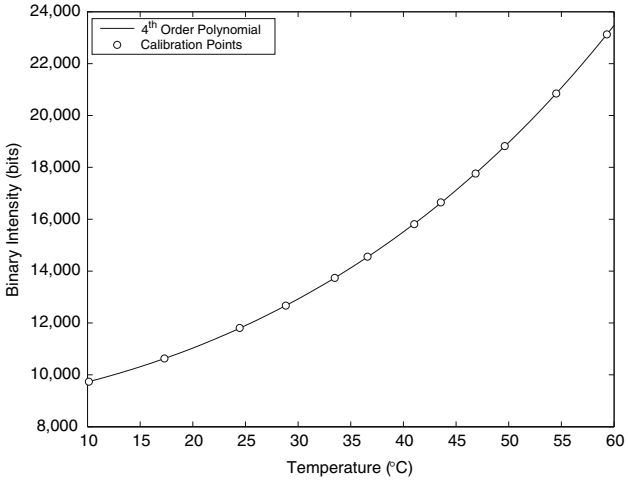

Fig. 5 Calibration of the 12-bit output of the digital infrared camera

To measure the water surface temperature for a given pixel, the reflection and calibration equations are simply inverted. From the measured intensity I_{12}, the equivalent water surface blackbody intensity is

$$I(T_s) = \frac{1}{\varepsilon}(I_{12} - (1 - \varepsilon)I(T_{Bk})). \quad (4)$$

Then the water surface temperature is obtained by inverting Eq. (2) numerically to give T_s.

The possibility of storing the 12-bit camera output was only recognized after a part of our experimental data were acquired. Accordingly, some of the imagery acquired for these experiments is in an 8-bit format where a portion of the 12-bit range is mapped from 0 to 255.

An error propagation analysis for the RMS temperature measurements obtained from the IR camera, which

[1] The camera manual consistently refers to these as 12-bit images possibly to recognize accuracy limitations in the data. However the data are represented as 16 bit numbers. We will refer to these images as 12-bit images, and refer to their pixel intensities as I_{12}, hereinafter.

included the random error, systematic error and calibration error gave a value of ±0.077 K. A similar analysis for the heat flux gave an error of ±27.8 W/m^2.

2.2 Experimental procedure

To generate a flux of heat from the water to the air flow, the water in the tank was initially heated to a temperature above the air temperature. Each experiment began by filling the tank with hot tap water, and heating it further if necessary for the high heat flux cases. The tank was initially filled to a level 3 mm or so below the rim to prevent wind-driven resonant waves that tended to occur if the tank was filled completely to the brim. A ruler was fastened to the side of the tank to measure the water level and record any water that was lost by evaporation. The blower was started and throttled to the desired wind speed, and then run for 15 min to allow the blower motor to achieve a steady-state temperature. The thermocouple logger was then started, recording T_p and T_b at 30 s intervals.

An experiment consisted of measuring temperatures, and acquiring infrared images, while the bulk temperature of the tank cooled off over a period of a few hours. This is an unsteady process, covering a range of decreasing fluxes. However, the unsteady process was slow enough that over short periods of time it could be considered a quasi-steady process. Sets of images were acquired over these relatively short periods of time, and an RMS was computed from these image sets. A heat flux was computed over the time interval corresponding to these image sets. Hence a (q'', σ) data point was obtained for each image set. Images were usually acquired once every 12 s during an image set, this being the fastest convenient frame rate supported by the camera. In some of the low heat flux cases, this rate was reduced to 1 image every 15 or 20 s because features in the IR imagery changed more slowly. Image sets typically consisted of 78–104 images and image acquisition lasted about 20 min.

2.3 Data reduction

Figure 6 shows a sample set of time traces for an experiment where the wind speed was 2.6 m/s which is used to illustrate the data reduction process. This figure shows the bulk temperature T_b, surface temperature T_s, and the plenum temperature T_p time traces. Only data from 5,000 to 10,000 s is presented in Fig. 6 for clarity. In Fig. 6, a dot is used to plot the mean value of each image acquired. These dots connect together to form line segments due to the large number of images. The means of all the images in each image set are plotted as single symbols (×) and each is plotted in the middle of the corresponding line segment. The length of each line segment corresponds to the duration of the image set. Between image sets there are gaps in time during which images were transferred to the computer or camera settings were adjusted, and therefore no T_s data were recorded. The ambient temperature, relative humidity and changes in water level were also recorded during these gaps.

The two quantities of primary interest in this study are the heat flux from the water surface q'', and the RMS σ of the surface temperature field. The heat flux measurement is based on the time rate of decrease for the bulk temperature. This is obtained from the time derivative of the curve fit to the bulk temperature data, as follows. An exponential curve fit was used having the form,

$$T_b(t) = (T_0 - T_a)e^{-t/\tau} + T_a, \tag{5}$$

where t is time, τ is the time constant for the exponential decay, T_0 is (nominally) the initial value of the bulk temperature, and T_a is (nominally) the asymptotic value of the bulk temperature. In practice, T_0 and T_a were used as optimization parameters in the fit. The sample plot presented in Fig. 6 shows that the curve fit matches the measured T_b within the envelope of its random scatter. Here, the RMS deviation of the T_b data and the T_b curve fit is 0.30°C.

The heat capacitance of the tank C includes contributions from the water and also the glass walls. The heat capacitance was allowed to vary with the volume $V(t)$ of water according to the measured fall of the water surface. The equation for C is,

$$C = \rho c_p V(t) + C_g \tag{6}$$

where ρ and c_p are the density and specific heat, respectively, of water, and C_g is the mass of the glass in the tank multiplied by its specific heat. The heat capacitance of the glass was computed to be C_g = 13,041 J/K. Multiplying C by the time derivative of Eq. (5), the total heat loss from the tank is

$$\dot{q}_{out} = C\frac{T_0 - T_a}{\tau}e^{-t/\tau}, \tag{7}$$

which includes both the loss from the air/water interface (the desired quantity), and the conduction loss through the tank walls $\dot{q}_{loss}$. This conduction loss is modeled as:

$$\dot{q}_{loss} = (T_b(t) - T_\infty)\kappa, \tag{8}$$

where κ is the conduction loss coefficient,

$$\kappa = 2.52\,\mathrm{W}/K \tag{9}$$

obtained from a test experiment in which the surface of the water tank was insulated to isolate the conduction loss. T_∞ is the ambient temperature which is modeled as

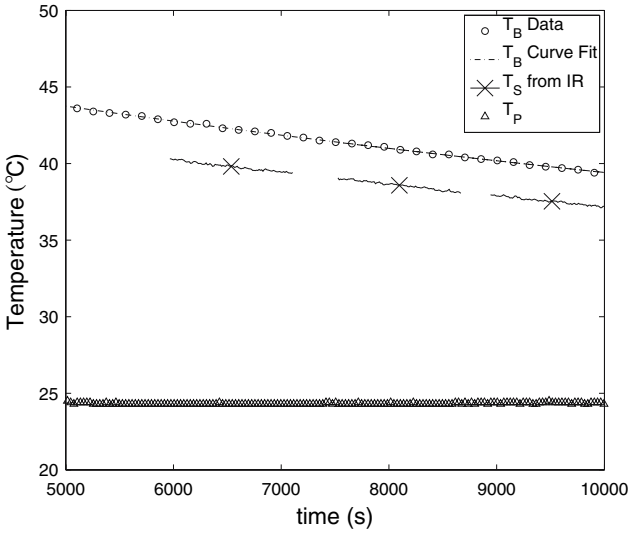

Fig. 6 An example of measured temperatures for a 2.6 m/s case. Only a portion of the total time interval of the experiment is presented in this figure. The length of each line segment with an × in its center corresponds to the length of the image set. The *gap* between these image sets corresponds to the time when images were transferred to the computer. T_b and T_p were recorded continuously. Note that only every fifth T_b data point is plotted here to prevent obscuration of the curve fit

$T_\infty = \overline{T_p} - 1.5°C$. (In another test experiment, the blower was found to elevate T_p above the ambient by 1.5°C). Finally, the desired heat flux across the air water interface, q'', is obtained from $\dot{q}_{loss}$ and $\dot{q}_{out}$ from the equation:

$$q'' = \frac{\dot{q}_{out} - \dot{q}_{loss}}{A_s}, \tag{10}$$

where A_s is the area of the air/water interface which was 0.253 m^2. All values of q'' presented here were obtained from Eq. (10).

As noted above, image sets consisted of 78–104 frames. Each set spanned roughly 20 min of run time, and it was reasoned that during this relatively short period of time the character of the flow would not change significantly, and that a single measurement of the RMS of the surface temperature σ would be valid and associated with a single value of q'' for the set.

The RMS of surface temperature was calculated relative to the decreasing expected value $\hat{T}(t)$. It was reasoned that calculating the RMS with respect to the mean computed by simply taking the average of the pixels in a given frame would unnecessarily sensitize the RMS to local (spatial and temporal) variations in the mean. Accordingly, the 'image mean temperature' was taken as the average temperature obtained from all of the images in the image set, adjusted by the decay in temperature obtained from the bulk temperature time trace, $\hat{T}(t)$. In other words, the mean surface temperature is modeled as decreasing linearly in time with a slope taken from the time derivative of the curve fit for T_b, at the middle of the image set (t_{set}) according to the equation:

$$\hat{T}(t) = \overline{T}_s - \frac{T_0 - T_a}{\tau} e^{-t_{set}/\tau}(t - t_{set}) \tag{11}$$

where $\overline{T}_s$ is the average temperature obtained from all pixels and all frames in the image set under consideration. Using $\hat{T}$ from Eq. (11), σ of the set was calculated according to

$$\sigma = \sqrt{\frac{\sum_{frames}\sum_{pixels}(T_{pixel} - \hat{T}(t))^2}{N_{frames}N_{pixels}}} \tag{12}$$

In a few test cases, the result of this method was compared with the result of the more common method of simply using the mean value of each frame when calculating σ. The value of σ resulting from the use of the special decreasing $\hat{T}(t)$ was slightly larger. For a typical run, (2.6 m/s, Run #7 in Table 1, below) the difference in the RMS computed using the two methods was 1.03%.

3 Results

A total of eighteen experimental runs were conducted for this study. Table 1 presents the wind speed and surface conditions for each run, along with the range of q'' and σ for that run. The goal of this work was to determine the effect of wind speed on the σ versus q'' relationship. To ascertain this wind speed effect, a constant surface condition must be maintained, since the presence or absence of a surfactant monolayer is known to affect σ (Saylor et al. 2001, 2000a). The approach taken here was to use the naturally occurring surfactant film that results from using tap water, to create a surfactant-covered condition for each run. This approach worked up to a wind speed of 2.6 m/s, above which the wind shear swept the monolayer partially downstream, creating a clean upstream region and a surfactant-covered downstream region, with a Reynolds ridge separating the two. This situation is undesirable since the measured value of σ would depend on whether the clean or surfactant-covered region was imaged. Additionally, the measured heat flux would be that due to an inhomogeneous surface condition. In an attempt to create a constant surfactant-covered condition at higher wind speeds, oleyl alcohol and Triton X-100 were applied to the tap water. These were runs 12 and 14–18, respectively, in Table 1. The attempts at using oleyl alcohol and Triton X-100 failed to create the desired uniformly covered surface. They are presented here for the sake of completeness. The oleyl

Table 1 Operating ranges of the 18 experimental runs

Run #	Condition (m/s)	q'' (W/m^2)	σ (°C)
1	1.0	567–1,998	0.297–0.715
2	1.0	691–1,736	0.295–0.589
3	1.0	698–1,732	0.277–0.533
4	1.0	364–520	0.184–0.253
5	1.0	164–231	0.138–0.149
6	1.8	892–1,253	0.282–0.350
7	2.6	730–1,456	0.294–0.399
8	2.6	588–1,503	0.261–0.403
9	2.6	696–1,732	0.291–0.450
10	2.6	284–522	0.154–0.205
11	2.6	120–273	0.132–0.158
12	4.0 Oleyl alcohol	576–1,534	0.194–0.349
13	4.0 Clean	697–1,587	0.186–0.303
14	1.0 Triton X-100	638–845	0.234–0.271
15	2.4 Triton X-100	789–909	0.270–0.294
16	2.4 Triton X-100	757–1,064	0.308–0.371
17	4.0 Triton X-100	847–988	0.103–0.109
18	4.0 Triton X-100	742–948	0.099–0.107

alcohol and Triton X-100 runs also revealed some interesting structure in the IR imagery, which will be described below, along with a small amount of imagery from a run that employed the solid phase surfactant, stearic acid. Runs listed in Table 1 lacking a surface condition notation are tap water runs.

Figure 7 shows the experimental results for all the tap water cases, presented as a plot of σ versus q'', calculated according to Eqs. (12) and (10), respectively. The values of q'' listed in Table 1 are the end-points of the corresponding lines in Fig. 7. Generally speaking, the data presented in Fig. 7 reveal a linear increase in σ with q''. While there is some differentiation in behavior at different wind speeds (as will be discussed further in Sect. 4), it could be argued that, to first order, the data fall on a single line, with a large degree of scatter. The deviation between wind speeds increases with q''.

The qualitative appearance of the IR imagery at the different wind speeds and heat fluxes investigated is of some interest. Some of the σ versus q'' data from Fig. 7 are replotted in Fig. 8 along with an oleyl alcohol run and a clean surface run. Annotations are included that indicate figure numbers where IR images are presented for sample values of wind speed and heat flux. In all of these IR images, the width of the image is 20.3 cm (the one exception to this is Fig. 11c and d, as indicated in the caption for that figure). The IR images for the runs presented in Fig. 8 are presented in Figs. 9, 10, 11. As Fig. 8 shows, IR images were selected at the lowest and highest

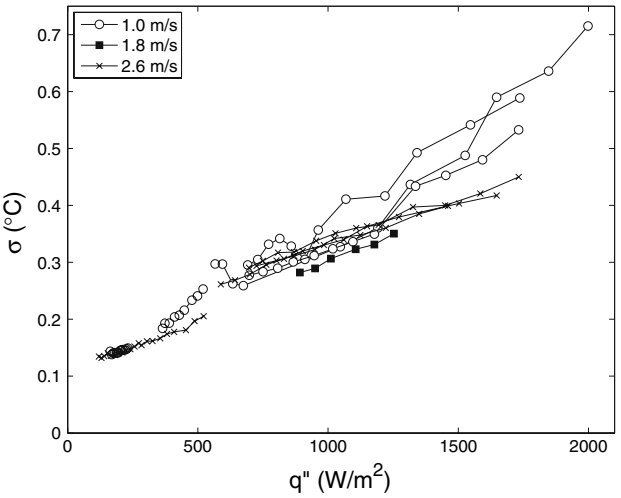

Fig. 7 Plot of σ versus q'' for the 1.0, 1.8, and 2.6 m/s tap water cases. Note that, as indicated in Table 1, each wind speed case may be comprised of more than one run. The data points for each run are connected by a *line*

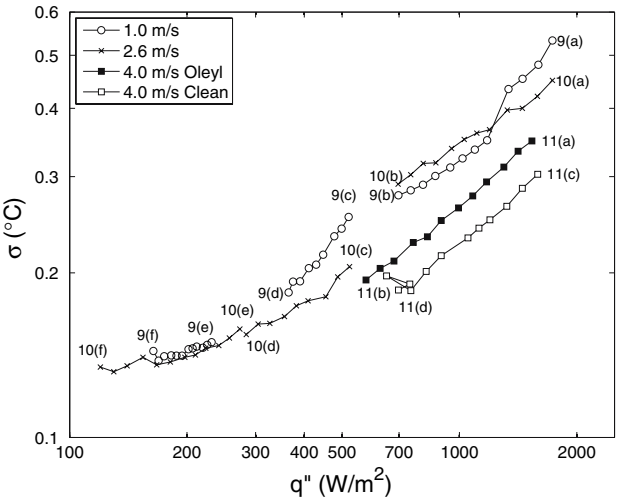

Fig. 8 Plot of σ versus q'' for selected runs. Annotations in the figure are keyed to subsequent figures where sample IR images taken at that particular (q'', σ) can be found: ○ refers to images in Fig. 9, × refers to images in Fig. 10, and □ and ■ refers to images in Fig. 11. log–log coordinates are used to separate the plots and better reveal the figure numbers

heat fluxes of each run (late and early in the run, respectively). The maximum and minimum temperatures are listed in Table 2 for each of the images presented in Figs. 9, 10, 11 and 13 (described later). These maximum and minimum temperatures correspond to a grayscale of white and black, respectively.

Figures 9 and 10 present IR images for tap water at 1.0 and 2.6 m/s, respectively. In both of these figures, it is clear that the structures are all aligned with the direction of the wind (top-to-bottom), as expected. As the heat flux

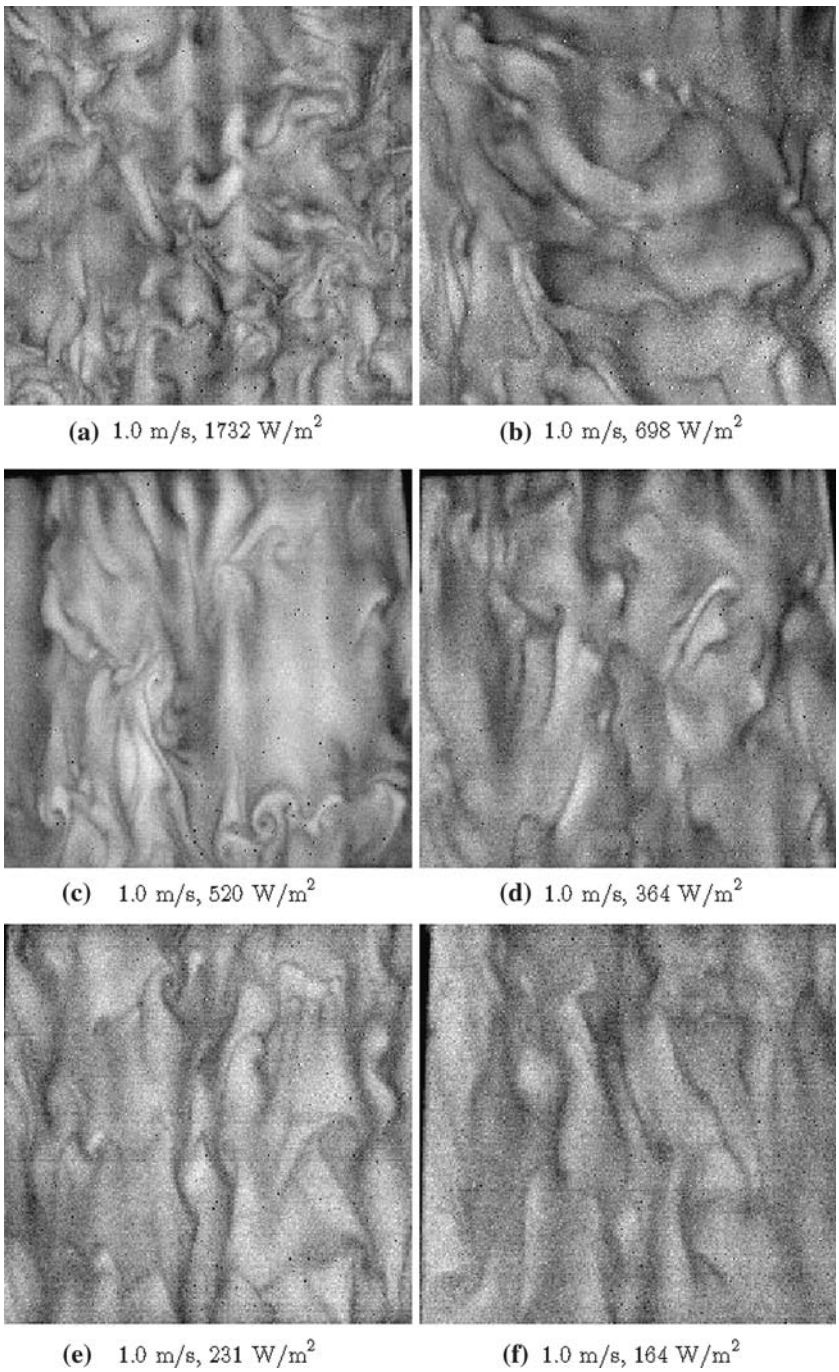

Fig. 9 Representative IR images from the tap water cases at 1.0 m/s for six different heat fluxes

increases at fixed wind speed, the spacing between structures decreases and the structures appear better defined. At constant heat flux (e.g., Figs. 9a and 10a), increasing the wind speed has the same effect, i.e., reduced spacing between structures, and better definition of structure.

As noted above, in an attempt to maintain a surfactant-covered surface at wind speeds above 2.6 m/s, oleyl alcohol was added to the indigenous surfactant film on the tap water surface. Oleyl alcohol was added in an amount of 0.6 μg per square cm of water surface. In spite of this relatively large amount of surfactant, the high shear stress at a wind speed of 4.0 m/s opened up a clean area, creating a Reynolds ridge located about 12″ downwind of the leading edge. While we were not able to maintain a completely homogeneous condition, we chose to record these images nevertheless to provide qualitative results of the surface temperature field under these relatively high wind speed conditions. To avoid imaging the Reynolds ridge, the camera was moved to a new location, 4″ downwind of its usual location at the middle of the tank in order to make sure the Reynolds ridge would not cross into the field of view, and the field of view would remain on a fully-covered surface. At this high wind

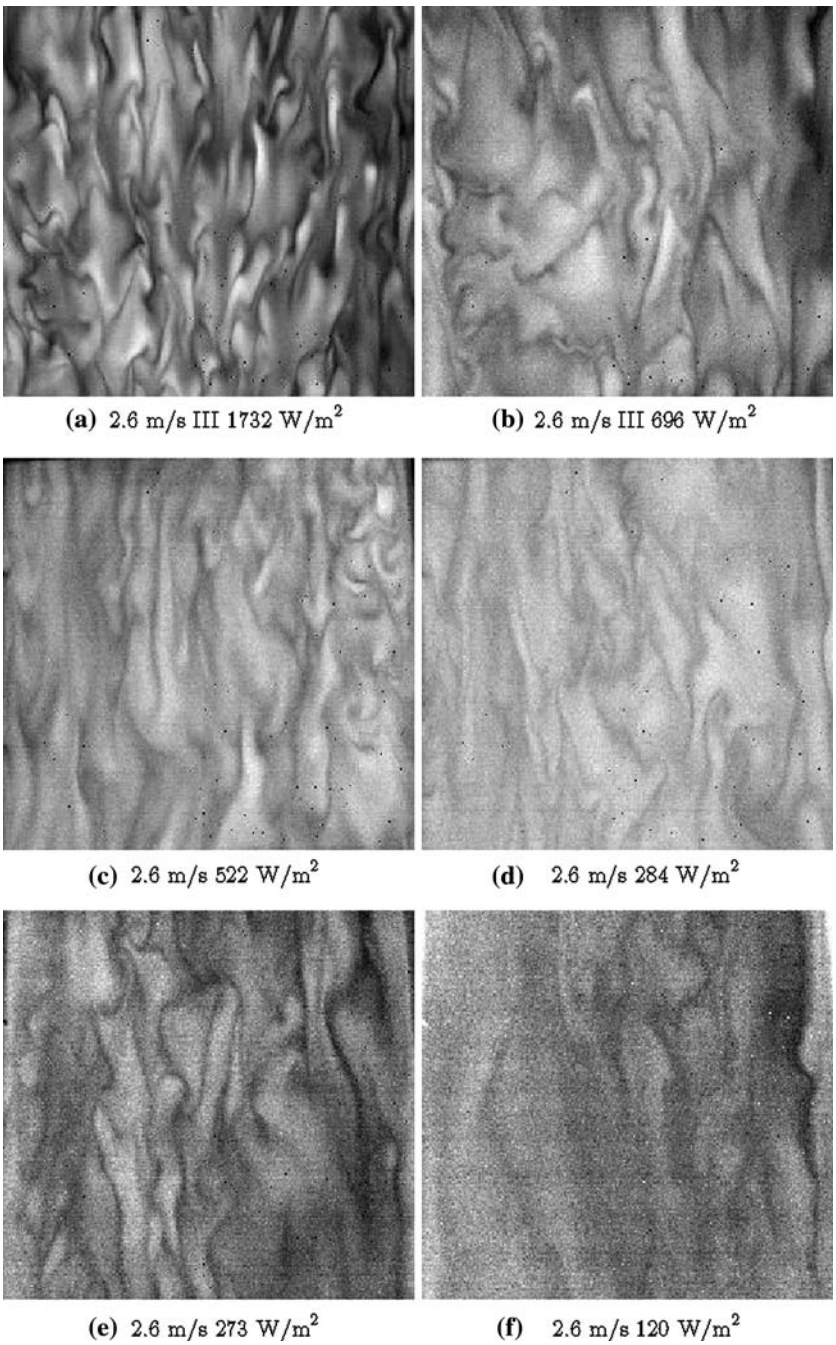

Fig. 10 Representative IR images from the tap water cases at 2.6 m/s, for six different heat fluxes

speed there were wind-driven ripples throughout the tank, though all the smaller-scale ones were damped out under the monolayer. The ripples had no visible effect on the infrared images. Fig. 8 shows the σ versus q'' data for the oleyl alcohol run. The plot of σ versus q'' in this case is much straighter than the tap water runs. Two sample IR images of these oleyl alcohol runs are presented in Fig. 11a and b at 1,534 and 576 W/m^2, respectively. Although the σ values for the oleyl alcohol run are significantly different from their tap water counterparts, the qualitative structure of the oleyl alcohol covered surface does not appear different from the tap water runs, the difference in wind speed notwithstanding.

To show how surfactants, in general, affect both σ and the qualitative IR structure, a clean surface condition run was conducted. The tank was cleaned prior to these experiments. Nevertheless, during the course of the experiment, new natural surfactant would collect at the downwind end, and it was removed by sweeping the downwind 30 cm or so of surface with a laboratory tissue

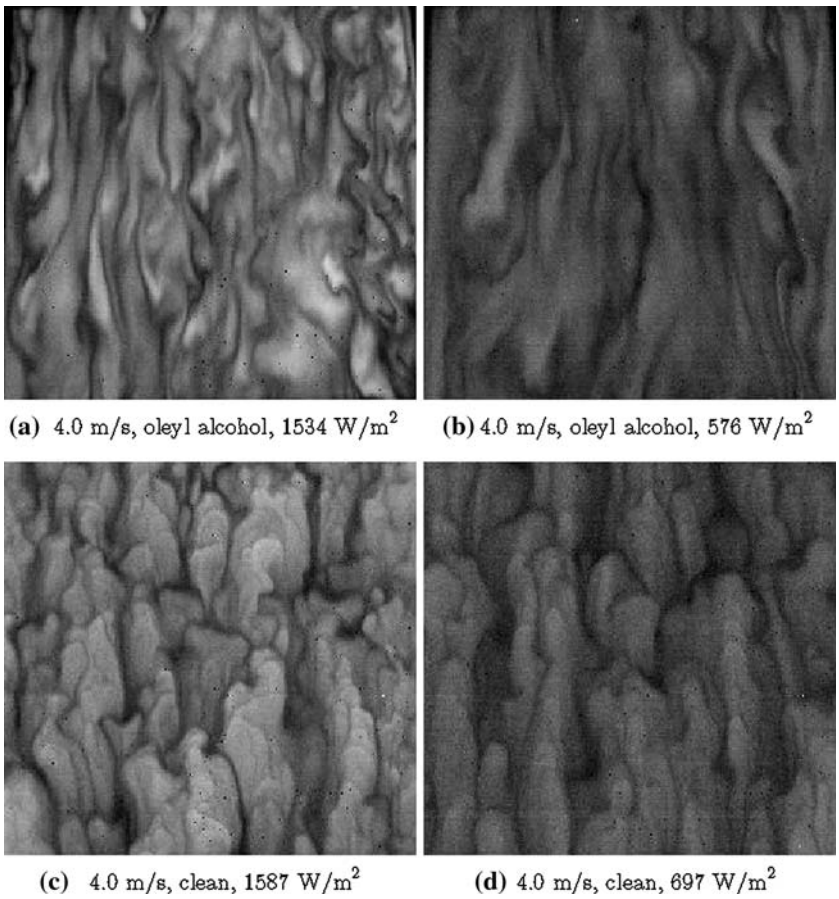

Fig. 11 Representative IR images from two cases. **a** and **b** 4.0 m/s with added oleyl alcohol to augment the natural surfactant monolayer. **c** and **d** 4.0 m/s with the surface kept clean. Note in the clean surface case the image scale is about half that shown in all the other cases. In each case two images are given, from early and late in the run (*left* to *right*)

(KimWipes) every 15 min. It was noted that the IR features re-established themselves quickly after a swipe so the next image acquired after the sweeping procedure was not noticeably affected. The flow features seen were consistent with the expected clean-surface features, guided by our earlier work at zero wind speed (Saylor 2001; Flack et al. 2001; Saylor et al. 2001; Saylor et al. 2000a, b).

As seen in Fig. 8, the σ measurements for the 4.0 m/s clean case is lower than both the 4.0 m/s oleyl case and the tap water case. The difference between σ for the 4.0 m/s clean and the 4.0 m/s oleyl case in Fig. 8 is comparable to the difference between the clean and oleyl alcohol σ shown in Fig. 1 for quiescent conditions. However, the trend is opposite in Fig. 1, with the clean condition exhibiting a higher RMS than the surfactant condition.

A much larger difference between the oleyl alcohol and clean case is seen in the qualitative appearance of the IR imagery as shown in Fig. 11. For example, Fig. 11a and c are taken at close to the same q'' and at the same wind speed. The features in the oleyl alcohol image are longer and 'stringier' in aspect ratio, while the features in the clean image are broader in appearance. Also, in the clean case, the warm features dominate the surface area and the cool features are relatively narrow boundaries between the warm features. Note that the scale of the clean images in Fig. 11 is about half that for the tap and oleyl images presented herein. The camera was moved closer to the water surface during the clean water runs due to the smaller length scales observed in these images. Hence, the physical size of the clean structures is smaller than their oleyl alcohol counterparts. Due to uncertainty in the cleaning procedure used here, detailed clean surface experiments were not conducted and the results presented here are for qualitative comparison only.

The soluble surfactant Triton X-100 was also tested in an attempt to provide a uniform surfactant-covered surface at wind speeds above 2.6 m/s. Because Triton X-100 is soluble, the surfactant molecules located in the monolayer are free to re-dissolve into the bulk, and vice-versa unlike the insoluble oleyl alcohol case. Figure 12 presents the σ versus q'' data for three of the five Triton X-100 runs. Due to the distinctly different behavior seen in the IR images, Triton X-100 was not investigated in great detail, and hence the data in Fig. 12 are sparse. Figure 12 also includes annotations keyed to Fig. 13 which contains sample IR images for the Triton-100 case. In these runs, 6.7 g of Triton X-100 was added directly to the tank to

Table 2 Values of the maximum and minimum temperatures for each of the IR images presented in Figs. 9, 10, 11 and 13

IR image	T_{max} (°C)	T_{min} (°C)	ΔT (°C)
Figure 9a	51.86	56.10	4.24
Figure 9b	37.45	39.56	2.11
Figure 9c	35.52	35.65	0.13
Figure 9d	31.34	32.69	1.35
Figure 9e	30.03	31.14	1.11
Figure 9f	26.57	27.72	1.15
Figure 10a	42.85	46.03	3.18
Figure 10b	29.02	31.22	2.22
Figure 10c	28.60	30.86	2.26
Figure 10d	24.73	26.99	2.26
Figure 10e	24.37	25.63	1.26
Figure 10f	21.86	23.05	1.19
Figure 11a	34.51	37.67	3.16
Figure 11b	25.79	28.65	2.86
Figure 11c	36.98	39.58	2.60
Figure 11d	27.40	29.71	2.31
Figure 13a	37.80	40.09	2.29
Figure 13b	32.17	35.13	2.96
Figure 13c	28.66	31.06	2.40

The last column presents the temperature range for each image, $T_{max} - T_{min}$

achieve about 1/3–1/2 of the critical micelle concentration (CMC). At 1.0 and 2.5 m/s the convective features observed in the IR imagery were similar to the natural surfactant or oleyl alcohol cases (which were very similar to each other), as shown in Fig. 13a and b. However, the Triton X-100 cases have a structure which is less oriented to the wind speed direction. Profoundly different behavior was observed for Triton X-100 at 4.0 m/s where the quasi-stationary monolayer was either swept away or replaced by a very elongated wind-driven monolayer as shown in Fig. 13c. As this figure shows, all the familiar structures seen in either the clean surface runs, tap water runs or oleyl alcohol runs are eliminated. As a check, the infrared camera was lowered to its minimum elevation, 12″ above the surface, and at that image scale there were still no apparent features (i.e., the same as shown in Fig. 13c). This sudden transition in behavior was very different from that observed in naturally occurring surfactants, and hence we abandoned Triton X-100 as a surfactant that could be used to bolster the naturally occurring surfactant in tap water.

Finally, the solid phase surfactant, stearic acid, was tested. For the stearic acid test, a solution of 1.4 mg stearic acid per ml of heptane was prepared, and applied sufficiently to cover the tank of warm water (20 drops or more). The stearic acid monolayer appeared rigid as

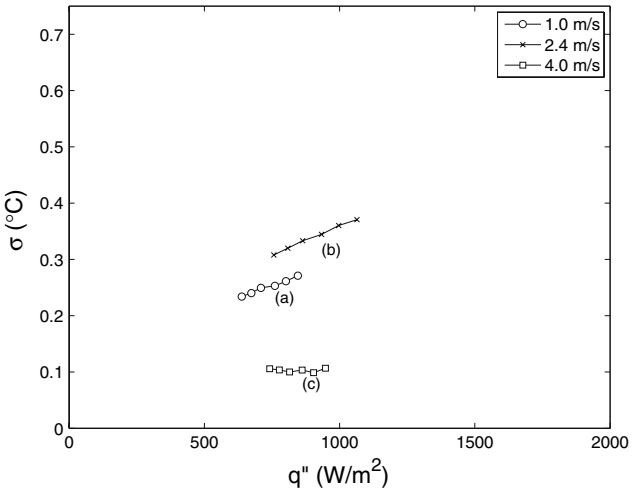

Fig. 12 Plot of σ versus q'' with *letters* keyed to the location of sample IR pictures presented for the Triton X-100 runs, which are found in Fig. 13

expected. At 1.0 m/s wind speed, the film was stable and large penetrative convection cells were visible in the IR imagery. At 2.5 m/s the film broke, exposing a small area of clean water surface. The crack in the monolayer gradually spread in a manner reminiscent of three-dimensional crack propagation. In the exposed area the characteristic clean-surface pattern of convection in the water was seen. Fig. 14 shows this situation. At 4.0 m/s the monolayer was entirely swept downwind. No quantitative measurements were taken for this surfactant.

4 Discussion

The goal of this study was to ascertain the effect of wind speed on the σ versus q'' relationship. The main results of this work can be found in Fig. 7 which presents plots of σ versus q'' for the tap water experiments. These plots show a roughly linear increase in σ with q''. Three wind speeds are presented in this figure. At low heat fluxes there seems to be little effect of wind speed on the σ versus q'' relationship. As the heat flux is increased, the plot shows a divergence between the 1.0 m/s runs and the 2.6 m/s runs, with the 2.6 m/s runs giving lower σ values than the 1.0 m/s runs. Quantifying the wind speed dependence in a more concrete fashion would require data at more wind speeds. However, as noted in the previous section, the surfactant monolayer was pushed downstream at wind speeds above 2.6 m/s. Doing experiments at finer wind speed intervals lower than 2.6 m/s was deemed unproductive since the scatter at constant wind speed would most likely have obscured any effect of wind speed over this range. Further progress in this area will require developing a method for

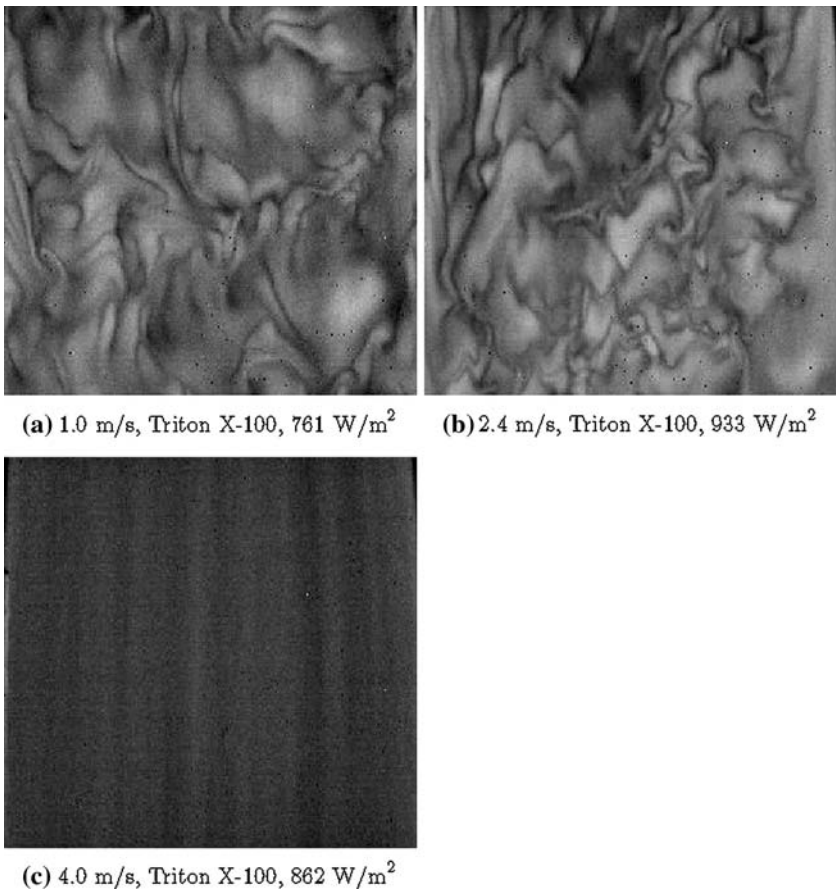

Fig. 13 Representative IR images from three different Triton X-100 cases, each at different wind speeds

maintaining a surfactant monolayer at wind speeds higher than 2.6 m/s.

The fact that the σ versus q'' plots in Fig. 7 appear independent of wind speed at low heat flux, and depend on wind speed at high heat fluxes, bears a closer look. The flow of air over the water surface in these experiments cools that surface to a temperature lower than the bulk water temperature. This is a buoyantly unstable situation which will result in natural convection in the water. Since the shear at the water surface creates a net surface water flow, there is also forced convection. Hence, the situation under study is one of mixed convection.

Mixed convection is quantified by the ratio of the Grashof number to the square of the Reynolds number, Gr/Re^2, which is a ratio of buoyant to inertial forces. The definitions of Grashof number (Gr) and Reynolds number (Re) used here are

$$Gr = \frac{g(\rho(T_b) - \rho(T_s))D^3}{\bar{\rho}v^2} \tag{13}$$

and

$$Re = \frac{VD}{v} \tag{14}$$

where the depth of the tank D was 38.10 cm (15″), and V is that characteristic water velocity which was taken to be 5% of the wind speed. Here Gr/Re^2 is computed for the water flow (as opposed to the air flow). Values of Gr/Re^2 less than one should correspond to the situation where forced convection dominates the flow and the heat transfer. In this situation, the air flow is driving the flow in the water via the shear at the air/water interface. It is expected that under these conditions the flow is steadier and more predictable since it is, ultimately, controlled by the blower. On the other hand, values of Gr/Re^2 greater than one correspond to situations where the wind is weak, and natural convection dominates the flow. This could be expected to be a less steady situation since convective cells in the water might meander, and small perturbations might change the global water flow in the tank, causing a lack of reproducibility and resulting in fluctuations in σ and q''.

Figure 15 is a plot of σ versus the ratio Gr/Re^2 for all of the tap water cases. Of all the experiments in this study, only the 1.0 m/s high-flux cases have $Gr/Re^2 > 1$. These are also the cases having σ versus q'' plots that show a great deal of variability in Fig. 7, suggesting that when natural convection begins to dominate the water flow, that flow becomes more prone to fluctuations. Hence, what this

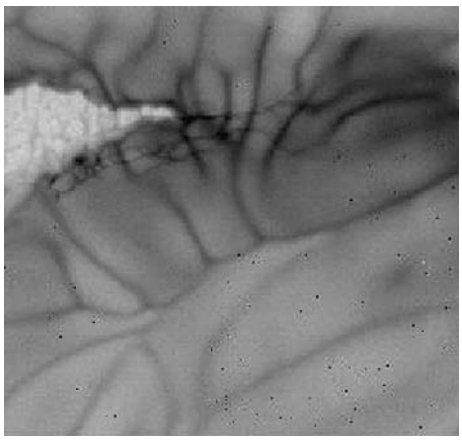

Fig. 14 A picture of a solid stearic acid monolayer at the inlet end of the tank. At 2.4 m/s the monolayer was beginning to fracture

seems to suggest is that the deviation of the σ values for different cases at high heat flux may not indicate a sensitivity to wind speed as much as a lack of reproducibility at high values of Gr/Re^2. While further experiments are needed to validate this, some evidence to support this idea can be seen in Fig. 9. This figure presents IR images of the tap water cases at 1 m/s over a range of heat fluxes. Although this wind speed is low, it can be seen that at the lower heat fluxes, the structures in the imagery are still oriented in the direction of the wind (e.g., Fig. 9e and f). However, at the high heat fluxes (e.g., Fig. 9a and b) the structures are less well oriented to the wind direction. It is possible that as the wind speed increases, and/or the heat flux decreases, the flow on the water side of the interface achieves a stable recirculating flow, dominated by the wind, and that at low wind speeds and/or high heat fluxes, the flow in the water is more random, dictated by the natural convection and therefore less reproducible.

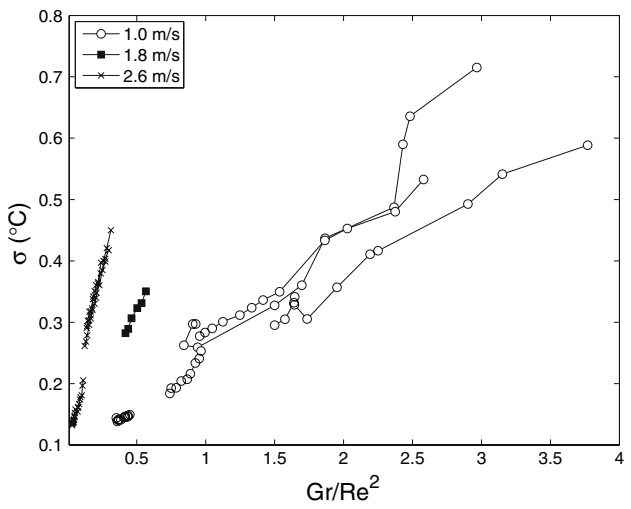

Fig. 15 The RMS σ versus the ratio Gr/Re^2 for all the tap water cases

Data obtained at different surfactant conditions are presented in Figs. 8 and 12. Because of the different surfactant conditions, comparison of these data will neither prove nor disprove whether variations in wind speed will spoil the linear relationship between σ and q''. These data sets consist of runs where the surfactants oleyl alcohol and Triton X-100 were added to bolster the naturally occurring surfactant film in the tap water.

The clean and oleyl alcohol data obtained at 4.0 m/s and presented in Fig. 8 show that, at constant heat flux, the RMS is consistently lower for the clean case when compared to the surfactant case. This is in contrast to the zero wind speed case presented in Fig. 1 for zero wind speed conditions. It is unclear why this is the case. It is possible that the presence of wind changes how surfactants affect the RMS of the surface temperature field. However, this cannot be a firm conclusion since for the 4.0 m/s oleyl alcohol case, the wind had pushed the monolayer partially downstream. While the IR camera was imaging only the surfactant-covered region (and hence the computed σ was for the surfactant region), the measured q'' was that due to a water surface that was partially covered with surfactant and partially uncovered.

The Triton X-100 experiments permitted us to maintain a surfactant monolayer at higher wind speeds, however the soluble nature of this surfactant seems to result in behavior that is clearly different from the naturally occurring surfactant, and this is evident in the IR imagery (Fig. 13c). Figure 12 shows a very significant effect of wind speed on the σ versus q'' plots for Triton X-100. But, again, it does not appear that this surfactant is similar in behavior to naturally occurring surfactants (e.g., the tap water cases). Finally stearic acid, a solid phase surfactant was also utilized, however it failed to provide a coherent film even at a wind speed of 2.4 m/s, as seen in Fig. 14, and plots of σ versus q'' were not obtained for this surfactant.

In oceanography, significant interest exists in the relationship between $\Delta T = T_b - T_s$, which is the difference between the temperature T_b that would be measured at depth via a buoy, for example, and the value of T_s that which would be measured remotely from a satellite (Castro et al. 2003). Relationships between ΔT and q'', and wind speed U have been investigated in great detail. While these relationships stray from the focus of the present paper, we briefly re-present our data here in a way that may provide some utility to researchers investigating sea surface temperature.

Saunders suggested that ΔT should be related to both q'' and U according to the equation (Saunders 1967):

$$\Delta T = \lambda \frac{q'' \nu}{k(\tau/\rho)} \tag{15}$$

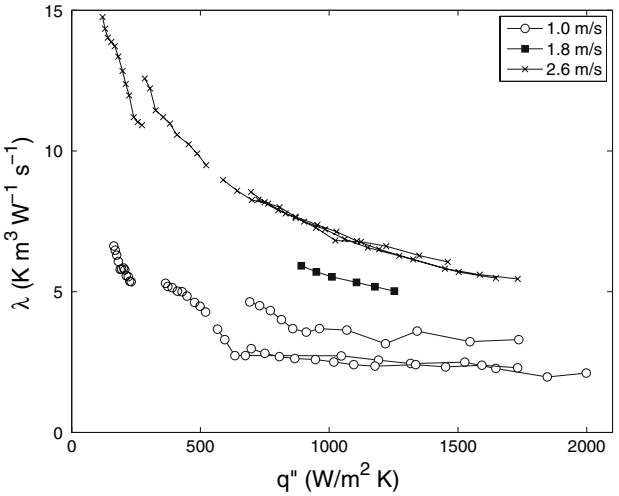

Fig. 16 Plot of λ (Eq. 15) versus q'' for each of the three wind speeds investigated. It is noted that the λ is dependent on both U and q''

where ν, k, and ρ are the kinematic viscosity, thermal conductivity, and density of water, and τ is the air-induced shear stress at the interface. In Eq. (15), λ is a proportionality constant. Much work has been done to ascertain the value of λ and to determine if it is in fact a constant. A good review of this work can be found in Wick et al. (1996) and Castro et al. (2003). In Fig. 16 we present our data plotted in the form of λ versus q''. As this figure shows, λ is not a constant and is indeed sensitive to both q'' and U''. The values range from 2 to 15, in general agreement with reported values (Saunders 1967; Wu 1985; Wick et al. 1996; Castro et al. 2003).

5 Conclusion

The results presented herein show to first order that the relationship between the RMS of the surface temperature field and the heat flux, for heat transfer from a warm body of water to an air flow, is not significantly affected by wind speed, at least up to a wind speed of 2.6 m/s. Fluctuations in the σ versus q'' data at large values of heat flux are hypothesized to be the result of variabilities that exist when natural convection is the dominant form of heat transfer. When forced convection controls the heat transfer, the σ versus q'' plots fluctuate less and are less sensitive to wind speed. Attempts to attain data at higher wind speeds were complicated by an inability to maintain a constant surfactant-covered condition for the entire water surface. The IR imagery obtained showed qualitative similarities for water surfaces contaminated by the indigenous surfactant found in tap water, and for monolayers of oleyl alcohol. Clean water surfaces showed significantly different structures in the IR imagery, as did a surface contaminated with the soluble surfactant, Triton X-100.

Acknowledgments This work was supported by the Department of Energy through the Savannah River National Laboratory.

References

Adamson AW (1990) Physical chemistry of surfaces. Wiley, New York

Bodenschatz E, Pesch W et al (2000) Recent developments in Rayleigh-Bénard convection. Ann Rev Fluid Mech 32:709–778

Boelter LMK, Gordon H et al (1946) Free evaporation into air of water from a free horizontal quiet surface. Ind Eng Chem 38:596–600

Castro SL, Wick GA et al (2003) Further refinements to models for the bulk-skin sea surface temperature difference. J Geophys Res 108:3377

Chuck W, Sparrow EM (1987) Evaporative mass transfer in turbulent forced convection duct flows. Int J Heat Mass Transf 30:215–222

Flack KA, Saylor JR et al (2001) Near surface turbulence for evaporative convection at an air/water interface. Phys Fluids 13:3338–3345

Garrett AJ (2002a) Power retrievals from multispectral thermal imager (MTI) images of the Comanche Peak steam electric station. Tech. Rep. SRTC-NA-2002-02, Savannah River National Laboratory, Savannah River Technology Center, Aiken

Garrett AJ (2002b) Power retrievals from multispectral thermal imager (MTI) images of the Pilgrim Nuclear Power Station. Tech. Rep. SRTC-NA-2002-03, Savannah River National Laboratory, Savannah River Technology Center, Aiken

Garrett AJ, Hayes DW (1997) Cooling lake simulations compared to thermal imagery and dye tracers. J Hydr Eng 123:885–894

Garrett AJ, Irvine JM et al (2000) Application of multispectral imagery to assessment of a hydrodynamic simulation of an effluent stream entering the Clinch River. Photogramm Eng Remote Sens 66:329–335

Gettling AV (1998) Rayleigh-Bénard Convection. World Scientific, Singapore

Katsaros KB, Liu WT et al (1977) Heat transport and thermal structure in the interfacial boundary layer measured in an open tank of water in turbulent free convection. J Fluid Mech 83:311–335

Nunez GA, Sparrow EM (1988)Models and solutions for isothermal and non-isothermal evaporation from a partially filled tube. Int J Heat Mass Transf 31:461–477

Parker FL, Krenkel P (1969) Thermal pollution: status of the art. Vanderbilt University

Prata AT, Sparrow EM (1985) Forced convection evaporation from a cavity containing a liquid whose surface is curved by capillarity: computations in interlocking rectangular and cylindrical domains. Numer Heat Transf 8:667–688

Prata AT, Sparrow EM (1986) Evaporation of water from a partially filled, cylindrical container to a forced convection air flow. Int J Heat Mass Transf 29:539–547

Saunders PM (1967) The temperature at the ocean–air interface. J Atmos Sci 24:269–273

Saylor JR (2001) Determining liquid substrate cleanliness using infrared imaging. Rev Sci Instrum 72:4408–4414

Saylor JR, Smith GB et al (2000a) The effect of a surfactant monolayer on the temperature field of a water surface undergoing evaporation. Int J Heat Mass Transf 43:3073–3086

Saylor JR, Smith GB et al (2000b) Infrared imaging of the surface temperature field of water during film spreading. Phys Fluids 12:597–602

Saylor JR, Smith GB et al (2001) An experimental investigation of the surface temperature field during evaporative convection. Phys Fluids 13:428–439

Sharpley BF, Boelter LMK (1938) Evaporation of water into quiet air from a one-foot diameter surface. Ind Eng Chem 30:1125–1131

Siggia ED (1994) High Rayleigh number convection. Annu Rev Fluid Mech 26:137–168

Sparrow EM, Kratz GK et al (1983) Evaporation of water from a horizontal surface by natural convection. J Heat Transf 105:469–475

Sparrow EM, Nunez GA (1988) Experiments on isothermal and non-isothermal evaporation from partially filled, open-topped vertical tubes. Int J Heat Mass Transf 31:1345–1355

Volino RJ, Smith GB (1999) Use of simultaneous IR temperature measurements and DPIV to investigate thermal plumes in a thick layer cooled from above. Exp Fluids 27:70–78

Wick GA, Emery WJ et al (1996) The behavior of the bulk skin sea surface temperature difference under varying wind speed and heat flux. J Phys Oceanogr 26:1969–1988

Wu J (1985) On the cool skin of the ocean. Bound Layer Meteorol 31:203–207